Prediction of basin-scale river channel migration based on landscape evolution numerical simulation

Jitian Wu[1], Xiankui Zeng[1], Qihui Wu[1], Dong Wang[1], and Jichun Wu[1]

[1] Key Laboratory of Surficial Geochemistry, Ministry of Education, School of Earth Sciences and Engineering, Nanjing University, Nanjing 210023, China

Correspondence: Xiankui Zeng (xiankuizeng@nju.edu.cn)

Abstract

The basin-scale river channel migration, driven by multiple factors such as hydrometeorological conditions, tectonic movements, and human activities, exerts a profound influence on regional morphological features, water resource, and ecosystem over long-term evolution. Conventional river dynamics approaches struggle to quantitatively characterize basin-scale channel migration due to difficulties in incorporating factors like basin hydrological processes and tectonic activities. This study proposed a novel technique for the numerical simulation of river channel migration, integrating a fully coupled multi-processes landscape evolution model (e.g., hydrological, geomorphic and tectonic processes) with channel extraction. Furthermore, to address model parameter uncertainty, a Markov chain Monte Carlo (MCMC) method with a modified likelihood function is used for parameter uncertainty quantification. Simultaneously, a computationally efficient Long Short-Term Memory (LSTM)-based surrogate model for channel migration is developed to overcome the computational bottleneck in uncertainty analysis. Applied to the Kumalake River Basin within China's Tarim Basin, the study employs the Landscape Evolution-Penn State Integrated Hydrologic Model (LE-PIHM) to construct the landscape evolution model. Combined with channel extraction, it simulates historical (2000-2021) and future (2021-2100) landscape evolution and channel migration processes. Results demonstrated that the developed river channel migration model, aided by parameter uncertainty analysis, reliably captures the dynamics of channel migration in the study area during 2000-2021. Additionally, the LSTM-based surrogate model achieves high accuracy, effectively resolving computational challenges in parameter uncertainty analysis. Predictions under different climate scenarios

33   reveal significant variations in future channel evolution, indicating that climate change will

34   profoundly reshape basin geomorphic features and river patterns.

35

1. Introduction

Basin-scale river channel migration is the result of interactions among multiple spheres within the complex earth system, influenced by various factors including meteorological, hydrological, and geological conditions (Li et al., 2023; Desormeaux et al., 2021). Over long temporal and basin scales, river channel migration regulates the spatial configuration of river networks, exerting significant impacts on regional water resources, ecological environments, and the development of civilizations. For instance, the substantial downstream migration of the Euphrates River between approximately 2112–2004 BCE contributed to the collapse of the Sumerian civilization (Hritz et al., 2010). The diversion of the lower Tarim River in 630 CE led to the disappearance of the ancient Loulan Kingdom (Yu et al., 2016; Shao et al., 2022). Quantitative research on river channel migration at the basin scale is crucial; it can not only inform projections of water resource distribution under climate change scenarios but also facilitate the reconstruction of linkages among channel evolution, fluvial ecosystems, and the trajectories of human civilizations (Hickin 1983; Zhou et al., 2022; Zhen et al., 2025).

River channel migration in the basin scale involves multiple coupled processes including surface water and groundwater water, weathering and erosion, and tectonic uplift. In particular, groundwater flow under real-world complex conditions may exhibit multi-scale heterogeneity (Lu et al., 2023). Together, these processes operate across broad spatiotemporal scales, exhibit complex mechanistic interactions, and are highly susceptible to anthropogenic disturbance. Numerical modeling therefore serves as the principal approach for quantitatively characterizing these dynamics. Among various modeling strategies, river channel migration models grounded in fluvial dynamics have been widely

59 used. For example, Ikeda et al. (1981) developed a single meander segment model by

60 coupling flow fields with erosion rates. Morón et al. (2017) employed Delft3D (Lesser et

61 al., 2004) to simulate the evolution of channel segments in the Nile River, Columbia River,

62 Congo River and Negro River. Hsu et al. (2022) utilized Nays2DH (Ali et al., 2017) to

63 simulate braided river morphology in the lower Dajia River, and identified that channel

64 width as a primary factor governing migration direction. However, these methods generally

65 focus on partial river channel domains (e.g., meander reaches) and fail to incorporate

66 hydrologic processes and tectonic activities at the basin scale, thus limiting their

67 applicability to river channel migration over engineering timescales and channel segment

68 scales.

69   As a typical geomorphic unit, river channels are fundamentally governed by landscape

70 evolution processes (Lisenby et al., 2020). Landscape evolution models (LEMs) are

71 numerical tools designed to quantify elevation changes across watersheds over geological

72 timescales, incorporating hydrologic processes and tectonic uplift (Bishop, 2007; Tucker

73 and Hancock, 2010; Hou et al., 2025). By integrating LEMs with river channel extraction

74 techniques, it becomes feasible to simulate long-term, basin-scale channel migration.

75 Commonly used LEMs include CASCADE (Braun et al., 1997), CHILD (Tucker et al.,

76 2001), CAESAR-Lisflood (Coulthard et al., 2013), DAC (Goren et al., 2014; Yang et al.,

77 2015), Landlab (Barnhart et al.,2020; Litwin et al.,2024), all of which have been widely

78 used for simulating landscape evolution. Nevertheless, these models often simplify or

79 neglect groundwater dynamics and lateral erosion processes (Whipple et al., 2017), making

80 it difficult to accurately capture these crucial hydrological and geomorphic processes in

81 large-scale, long-term watershed landscape evolution simulations.

82   Zhang et al. (2016) developed LE-PIHM by coupling surface-subsurface

83   hydrologic processes with slope and channel sediment transport, while accounting for

84   bedrock weathering and tectonic uplift, based on the PIHM framework (Qu et al., 2007).

85   LE-PIHM is particularly suited for quantifying landscape evolution processes over long

86   durations and basin extents. Nevertheless, current studies rarely integrate multiple

87   processes for real basin-scale simulations of coupled landscape evolution and river channel

88   migration. Meanwhile, LEMs contain a large number of parameters to be identified, the

89   non-negligible parameters uncertainty can lead to unreliable simulations of landscape

90   evolution and river channel migration, which has not been adequately addressed in current

91   researches (Temme et al., 2009; Neuendorf et al., 2018; Xu et al., 2024). To quantify river

92   channel migration at the basin scale under the coupled effects of multiple processes, the

93   LE-PIHM was used to establish a landscape evolution model in this study, and the

94   distribution of river channels was identified using a river channel extraction technique. In

95   addition, Long Short-Term Memory (LSTM) surrogate modeling and Bayesian uncertainty

96   analysis were employed to quantify parameter uncertainty in the LEMs.

97   This study selects the Kumalake River Basin within China's Xinjiang Tarim Basin as

98   the research area. This basin features diverse geomorphic types and complex climatic

99   conditions, and has experienced significant river channel migration in recent decades

100   (Wang et al., 2024), making it an ideal site for conducting basin-scale simulations of terrain

101   evolution and river channel dynamics. Based on the identified model parameters

102   distribution of LE-PIHM, the river channel migration process in the study area over the

103   past two decades was quantitatively reconstructed. Finally, this study conducted future

104   scenario simulations of landscape evolution and river channel migration under projected

105   climate change through the end of the 21st century.

106   The structure of this paper is as follows: Sect. 2 outlines the methodology and overall

107   workflow; Sect. 3 introduces the construction of the basin-scale river channel migration

108   model and the development of an LSTM-based surrogate model for uncertainty analysis;

109   Sect. 4 presents the results and discussion; and Sect. 5 provides concluding remarks and

110   summarizes the key findings.

2. Methodology

2.1 Framework of basin-scale river channel migration prediction

113   The framework of predicting basin-scale river channel migration in this paper consists

114   of three parts (Fig.1).

115   Part 1: Establishment of the basin-scale river channel migration model. The basin-

116   scale river channel migration model is implemented in two steps. First, landscape evolution

117   is simulated using LE-PIHM to obtain the elevation distribution of the study area.

118   Subsequently, the DEM is processed using the D8 algorithm to extract the spatial

119   distribution of river channel.

120   Part 2: Development of a LSTM-based surrogate model for efficient parameter

121   uncertainty analysis. To improve the efficiency of parameter identification, a surrogate

122   model corresponding to the original river channel migration model (Part 1) is developed

123   for the reconstruction period (2000–2021). Parameter sensitivity analysis is first conducted

124   to identify the key landscape evolution parameters of LE-PIHM. Then, 3,000 parameter

125   sets are sampled and input into the basin-scale river channel migration model (Part 1) to

126   generate the associated planar channel coordinates, which serve as the training datasets.

127   The LSTM is trained using these data to construct a surrogate model of basin-scale river

128 channel migration, substantially reducing the computational burden of parameter

129 uncertainty analysis.

130   Part 3: Parameter uncertainty analysis and the prediction of channel migration. Based

131 on the LSTM-based surrogate model (Part 2), parameter uncertainty analysis is conducted

132 using a modified-likelihood Markov chain Monte Carlo (MCMC) approach constrained by

133 observed river channel data from 2000 to 2021. The resulting posterior distribution of river

134 channel enable the reconstruction of channel migration processes over 2000–2021. The

135 maximum-likelihood posterior parameter set is then selected, and the original river channel

136 migration model (Part 1) is executed under future climate scenarios to predict channel

137 migration from 2021 to 2100.
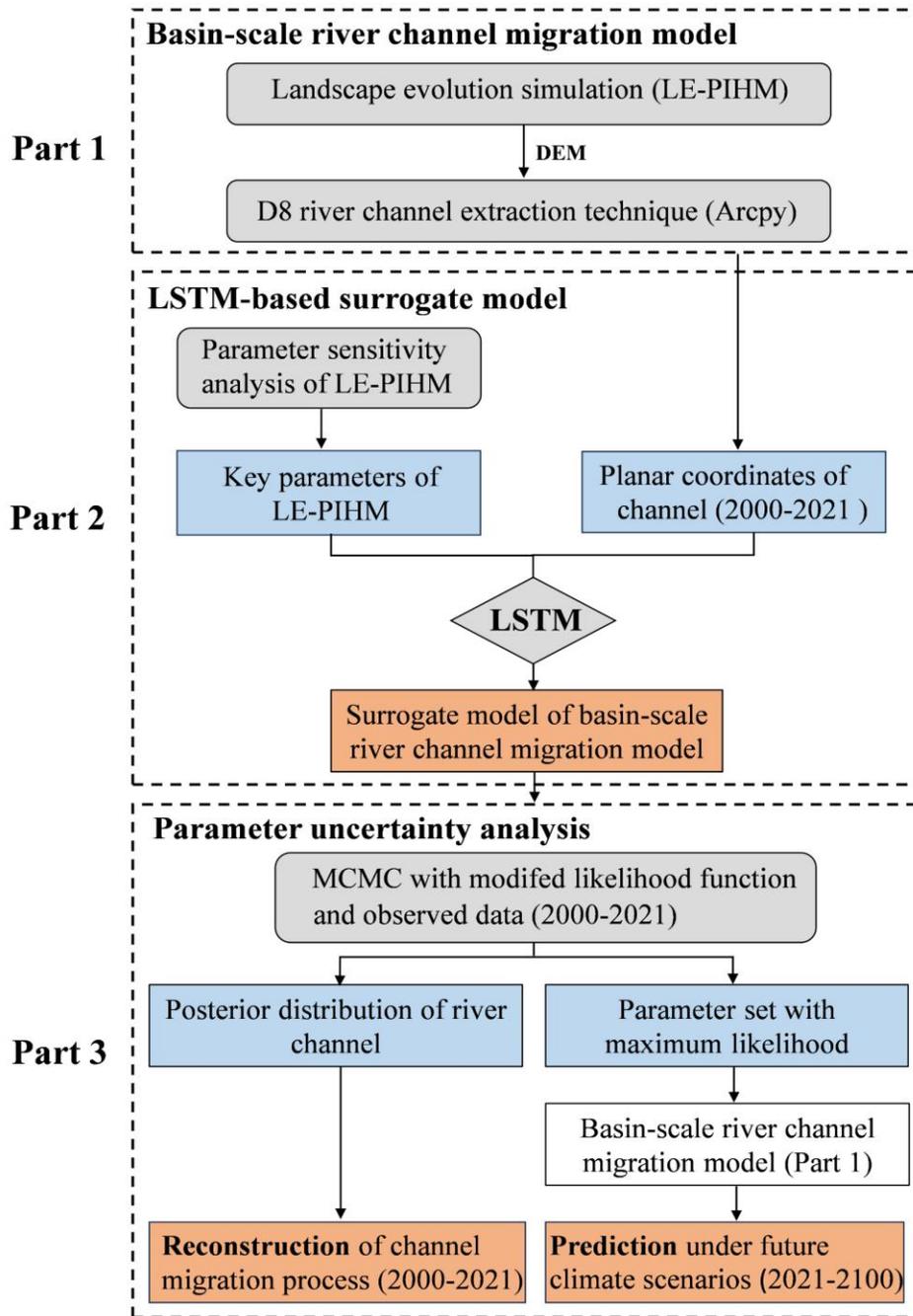
Figure 1. Technical roadmap of basin-scale river channel migration prediction

2.2 Basin-scale river channel migration model

2.2.1 Landscape evolution simulation

The Landscape Evolution–Penn State Integrated Hydrologic Model (LE-PIHM) was

used to simulate the landscape evolution processes. LE-PIHM couples the processes of

144   surface water and groundwater, snow accumulation and melt, hillslope and river channel

145   sediment transport, weathering and erosion, as well as tectonic uplift (Fig. 2). It is a basin-

146   scale fully coupled hydrologic-process-based landscape evolution model (Zhang et al.,

147   2016). The hydrologic and geomorphic modules are tightly coupled within the same control

148   volume through mass conservation and flux closure, and the state variables are updated

149   synchronously at each time step. For each grid element (a Triangulated Irregular Network,

150   TIN), the model simultaneously tracks seven state variables: canopy water storage,

151   snowpack, surface-water depth, vadose-zone water storage, saturated-zone groundwater

152   table, land-surface elevation, and bedrock-interface elevation. These state variables are

153   assembled into a unified global system of ordinary differential equations and are solved

154   concurrently. Within each TIN control volume, multiple fluxes including infiltration,

155   recharge, overland flow, groundwater flow, and sediment/weathering/uplift fluxes coexist

156   and are transported in a coupled manner across the entire TIN mesh domain.

157   The model simulates surface elevation change based on the principle of mass

158   continuity. According to the law of mass conservation, the geomorphic process equation

159   can be expressed as the temporal variation of the mass of the regolith and bedrock.

160

$$
\begin{aligned}
\frac{\partial(\sigma_{re}h\mathrm{d}x\mathrm{d}y)}{\partial t} + \frac{\partial(\sigma_{ro}e\mathrm{d}x\mathrm{d}y)}{\partial t} = &\ \sigma_{re}q_c\mathrm{d}y - [\sigma_{re}q_c\mathrm{d}y + \frac{\partial(\sigma_{re}q_c\mathrm{d}y)}{\partial x}\mathrm{d}x] \\
& + \sigma_{re}q_c\mathrm{d}x - [\sigma_{re}q_c\mathrm{d}x + \frac{\partial(\sigma_{re}q_c\mathrm{d}y)}{\partial y}\mathrm{d}y] \\
& + \sigma_{re}q_s\mathrm{d}y - [\sigma_{re}q_s\mathrm{d}x + \frac{\partial(\sigma_{re}q_s\mathrm{d}y)}{\partial y}\mathrm{d}x] \\
& + \sigma_{re}q_s\mathrm{d}x - [\sigma_{re}q_s\mathrm{d}x + \frac{\partial(\sigma_{re}q_s\mathrm{d}y)}{\partial y}\mathrm{d}y] \\
& \ \sigma_{ro}U\mathrm{d}x\mathrm{d}y
\end{aligned}
\tag{1}
$$

161   where $\sigma_{re}$is the bulk density of regolith (kg/m³);$\sigma_{ro}$is the bulk density of bedrock (kg/m³);

162   h is the regolith thickness (m); e is the elevation of the bedrock surface (m); The regolith

163 thickness h is defined as the difference between the ground surface elevation z and the

164 bedrock elevation e; q_c is the lateral volumetric flux of regolith (m²/yr), driven by processes

165 such as soil creep; q_s is the surface sediment flux by overland flow (m²/yr); U is the tectonic

166 uplift rate (m/yr).

167   The governing equations for hydrologic processes describe the water flux dynamics

168 from the vegetation canopy to the regolith layer. These processes can be represented as

169 follows:

170
$$\begin{cases} \dfrac{\partial \psi_{\text{canopy}}}{\partial t} = \upsilon Frac(1 - f_{\text{s}})p - E_{\text{c}} - TF \\[2mm] \dfrac{\partial \psi_{\text{snow}}}{\partial t} = f_{\text{s}}p - SM \\[2mm] \dfrac{\partial \psi_{\text{surf}}}{\partial t} = \nabla q_{\text{sw}} + p_{\text{net}} - I - E_{\text{s}} \\[2mm] \dfrac{\partial \psi_{\text{unsat}}}{\partial t} = I - R - E_{\text{g}} - E_{\text{gt}} \\[2mm] \dfrac{\partial \psi_{\text{sat}}}{\partial t} = \nabla q_{\text{gw}} + R - E_{\text{sa}t} - E_{\text{tsat}} \end{cases} \tag{2}$$

171 where: Ψ_{canopy} is the canopy water storage (m); Ψ_{snow} is the snow depth (m); Ψ_{surf} is the

172 surface water depth (m); Ψ_{unsat} is the water storage in the unsaturated zone (m); Ψ_{sat} is

173 the groundwater (saturated zone) storage (m); $vFrac$ is the fraction of vegetation

174 coverage; f_s is the fraction of precipitation falling as snow; P is the precipitation rate

175 (m/day); E_c and E_s are the evaporation rates from the canopy and surface water, respectively

176 (m/day); TF is the throughfall rate from canopy to ground (m/day); SM is the snowmelt rate

177 (m/day); p_{net} is the net precipitation reaching the ground surface (m/day); I is the

178 infiltration rate (m/day); E_{g} and E_{sat} are the evaporation rates from the unsaturated and

179 saturated zones, respectively (m/day); E_{gt} and E_{tsat} are the transpiration rates from the

180 unsaturated and saturated zones, respectively (m/day); q_{sw} is the unit-width overland flow

181 rate (m²/day); q_{gw} is the unit-width groundwater (lateral) flow rate (m²/day).

182   The values of q_{sw} and q_{gw} are determined by the Manning equation and Darcy's law,

183 respectively, as follows:

184
$$q_{sw} = \frac{\psi_{surf}^{5/3}}{n_s}(\nabla(\psi_{surf}+z)^{)1/2}) \tag{3}$$

185
$$q_{gw} = \psi_{sat}k_{sat}\nabla(\psi_{sat}+e) \tag{4}$$

186 where n_s is the Manning's roughness coefficient; k_{sat} is the horizontal hydraulic

187 conductivity of the aquifer (m/day). For detailed formulas and variable descriptions, please

188 refer to Qu and Duffy (2007).

189   In summary, topography elevation and bedrock elevation determine hydraulic slopes

190 and head gradients, whereas hydrologic states (e.g., surface-water depth and groundwater

191 level) govern shear stress and sediment-transport capacity. Sediment fluxes (q_s), hillslope

192 fluxes (q_c), and uplift terms are solved in a coupled manner to update elevations, which in

193 turn modify hydraulic gradients and flow-routing patterns. This two-way feedback implies

194 that the evolving landscape constrains river dynamics, and river processes reshape the

195 landscape, thereby forming a self-consistent loop of hydro-geomorphic co-evolution.

196 Collectively, The governing equations (1-4) couple hydrological processes, hillslope and

197 channel sediment transport processes, and tectonic movements to form a state-of-the-art

198 hydro-geomorphic model for simulating landscape evolution.

199

200

201
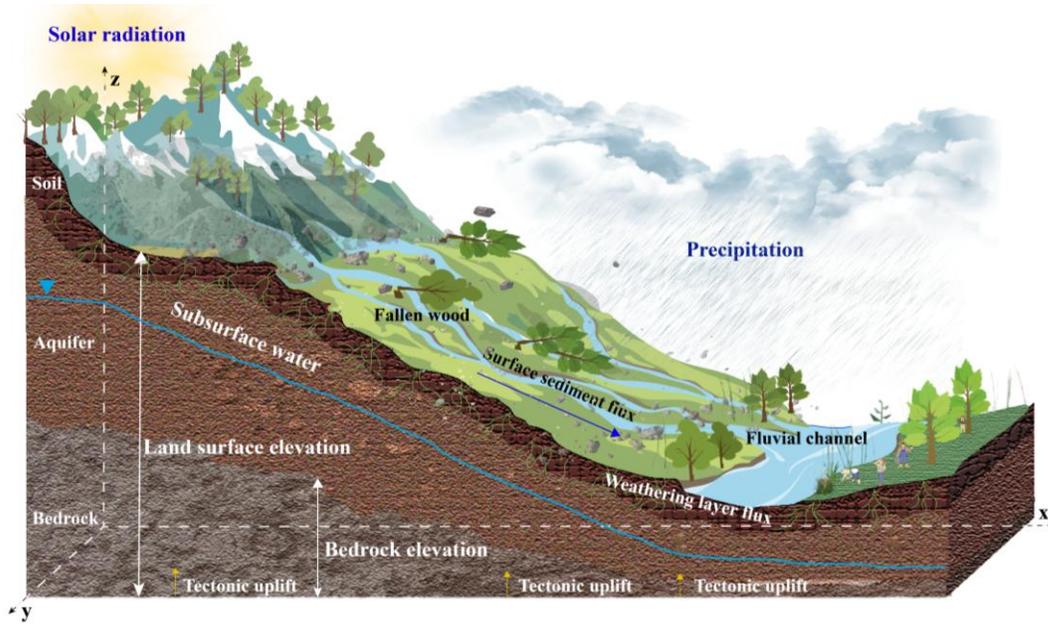
Figure 2. Schematic diagram of the Landscape evolution process.

2.2.2 D8 algorithm river channel extraction technique

The river channel extraction in basin-scale is implemented through a topography-based extraction technique. This technique is based on the principle of maximum gradient and identifies river channels within the watershed using surface elevation data. Specifically, the landscape evolution simulation provides the surface elevation distribution of the study area, from which a digital elevation model (DEM) is constructed. The DEM is first filled to remove depressions, followed by spatial analysis to determine surface flow direction and compute flow accumulation. River channel distribution is then extracted based on the accumulated flow.

The standard D8 algorithm, known for its simplicity and practicality, is currently the most widely used and reliable method for determining water flowpaths from DEM (O'Callaghan & Mark, 1984; Tarboton, 1997). The ArcPy scripting in ArcGIS, which implements the standard D8 algorithm (Esri, 2022), will be used in this study to extract watershed river channels through the ArcGIS hydrological analysis platform.

2.2.3 Long Short-Term Memory algorithm

Long Short-Term Memory (LSTM) is a specialized type of Recurrent Neural Network (RNN), originally proposed by Hochreiter et al. (1997) and later extended and popularized by Graves et al. (2005). Traditional RNNs often suffer from the vanishing or exploding gradient problem when processing long sequential data, making it difficult to capture long-term dependencies effectively. LSTM addresses this issue by introducing gated mechanisms namely the forget gate, input gate, and output gate, which dynamically regulate the flow of information. These gates allow the network to selectively store, update, and output information within memory cells, thereby effectively addressing the gradient instability problem in long-sequence modeling.

To address the computational burden caused by repeated model evaluations during the parameter uncertainty analysis of the basin-scale river channel migration model, this study constructs a surrogate model using an LSTM network. Specifically, the LSTM algorithm is employed to build the nonlinear response relationship between the key parameters of LE-PIHM and the spatial distribution of river channels (i.e., planar coordinates of reaches) within the study area.

2.3 Bayesian uncertainty analysis

2.3.1 Markov chain Monte Carlo simulation

Markov chain Monte Carlo (MCMC) is a statistical simulation technique based on Bayesian theory. Its core idea is to construct a Markov chain that iteratively explores the parameter probability space to generate samples from the target posterior distribution. As the chain evolves, its stationary distribution converges to the posterior distribution of the parameters of interest (Vrugt et al., 2009).

240   MCMC integrates observational data through Bayes' theorem, enabling parameter

241   samples to progressively converge from the prior distribution $p(\theta)$ to the posterior

242   distribution $p(\theta \mid D)$.

243
$$p(\theta \mid D) = \frac{L(\theta \mid D)p(\theta)}{\int L(\theta \mid D)P(\theta)d(\theta)} \tag{5}$$

244   where $L(\theta \mid D)$ represents the likelihood function of a parameter sample θ, D represents

245   the observed data. The likelihood function L is typically defined as a Gaussian likelihood

246   function:

247
$$L(\theta^i \mid D) = \frac{1}{2\pi^{n/2} \mid \Sigma \mid^{1/2}} \exp\left[-\frac{[D - f(\theta^i)]^{\mathrm{T}} \Sigma^{-1}[D - f(\theta^i)]}{2} \right] \tag{6}$$

248   where n is the number of observed data points, $f(\theta^i)$ denotes the hydrologic model

249   simulation result given the parameter θ^i, and Σ is the covariance matrix of the simulation

250   residuals.

251   2.3.2 Hausdorff distance and the modified likelihood function

252   The Hausdorff distance is employed as a metric to quantify the discrepancy between

253   the simulated and the observed river channels. The Hausdorff distance is a well-established

254   measure of curve-to-curve spatial similarity and has been widely applied in studies of river-

255   morphology matching, path comparison, and geomorphic feature shape analysis (Lei and

256   Lei, 2022; Bogoya et al., 2019; Ranacher and Tzavella, 2014). The Hausdorff distance

257   summarizes distances across all discretized points along the entire channel, thereby

258   accounting for both the overall displacement and differences in channel curvature and

259   planform geometry.

260   The core concept of the Hausdorff distance is to treat two curves as two sets of discrete

261   points (Fig. 3). Suppose we have two point-sets, $A = \{a_1, \ldots, a_p\}$, $B = \{b_1, \ldots, b_q\}$, p and q

262　represent the number of points in sets A and B, respectively, the bidirectional Hausdorff

263　distance HD(A, B) between sets A and B is defined as:

$$HD(A, B) = Max [h(A, B), h(B, A)] \qquad (7)$$

265　where h(A, B) and h(B, A) represent the one-sided Hausdorff distances. Specifically, h(A,

266　B) denotes the set of minimum distances from each point in set A to the nearest point in

267　set B, h(A, B) = $h(a_{1min}, a_{2min}, …, a_{pmin})$, where a_{1min} is the minimum distance from point

268　a_1 to the points in set B. Similarly, h(B, A) = $h(b_{1min}, b_{2min}, …, b_{pmin})$ which denotes the set

269　of minimum distances from each point in B to the nearest point in A.

270　　　　　　　　　　　*Calculate the average value of Hausdorff distance.*
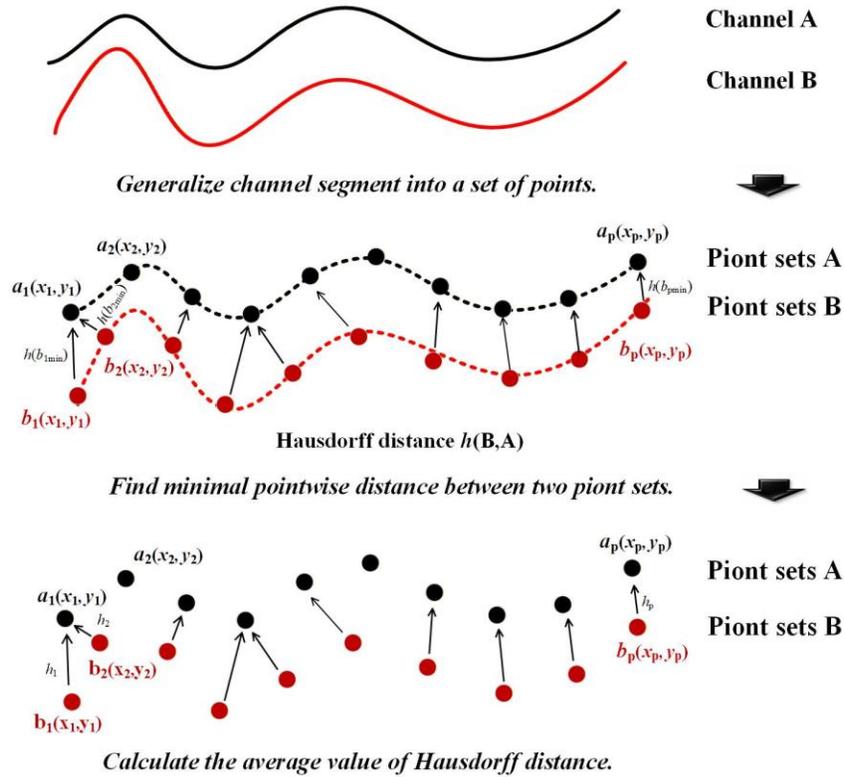
271　　　　　　　　　**Figure 3.** Conceptual schematic diagram of Hausdorff distance.

272　　　　In this study, we modified Eq. (7) by replacing the maximum operation in the one-

273　sided distance with the mean of the minimum distances, and set p equal to q. This

274　modification better captures the overall spatial discrepancy between two river channel

275　curves and is referred to as the average Hausdorff distance (*H*). A smaller value of *H*

16

276   indicates that the simulated river channel more closely matches the observed channel.

$$H = \frac{1}{2p} \sum_{i=1}^{p} [h(A,B) + h(B,A)] \tag{8}$$

278   In the uncertainty analysis of river channel migration simulation, the likelihood

279   function quantifies the degree of fit between the simulated and observed river channels. To

280   enable the parameter uncertainty quantification through MCMC, the original likelihood

281   function (i.e., Eq. (6)) is revised by treating the average Hausdorff distance (H) as the

282   simulation target. The observed value of H (denoted as H_{obs}) is set to 0, this indicates the

283   H between the real river channel and itself. Meanwhile, the Σ in Eq. (6) collapses to a single

284   variance term, and the residuals in likelihood function can be expressed as:

$$\mathrm{D} - f(\theta^i) = H - H_{obs} = H - 0 = H \tag{9}$$

286   The observation error of H_{obs} is treated as a random error variable that follows a zero-

287   mean, independent and identically distributed gaussian error model, i.e., N $(0, \sigma^2)$.

288   Combining Eq. (6) with Eq. (9) and taking the natural logarithm, a modified likelihood

289   function designed for quantifying river channel simulation is obtained:

$$\ln L = -\frac{1}{2} [\frac{H^2}{\sigma^2} + \ln(2\pi\sigma^2)] \tag{10}$$

291   In other words, this modified form of the likelihood function (Equation 10) is used in the

292   MCMC-based uncertainty analysis of river channel model parameters.

3. Construction of the river channel migration model

3.1 Study area

295   The Kumalake River Basin is located in the northwestern corner of the Tarim Basin

296   in Xinjiang, China, covering an area of about 3,500 square kilometers. The basin is

297   bordered by the towering Tianshan mountains to the north, the flat Aksu Plain to the south,

298   and the Toxkan River Basin to the west. The landscape exhibits a distinct elevation gradient

299   sloping from north to south, with a complex geomorphic setting comprising mountainous

300   hillslopes, valley plains, and fluvial terraces (Fig. 4). The Kumalake River, approximately

301   89.34 km in length, is the largest tributary of the Aksu River. It flows from the northwest

302   to the southeast across the study area and exits at the southeastern edge of the basin, where

303   it joins the Tuoshigan River. The combined flow continues into the Aksu River and

304   eventually discharges into the main stem of the Tarim River (Tang et al., 2007).

305   The Kumalake River has experienced pronounced channel migration during the last

306   two decades. This study selects the Kumalake River Basin as the case study area, with a

307   focus on simulating river channel migration over the period from 2000 to 2021. The

308   simulation is conducted within the landscape evolution modeling framework, and a

309   parameter uncertainty analysis is performed to improve the reliability of the model outputs.
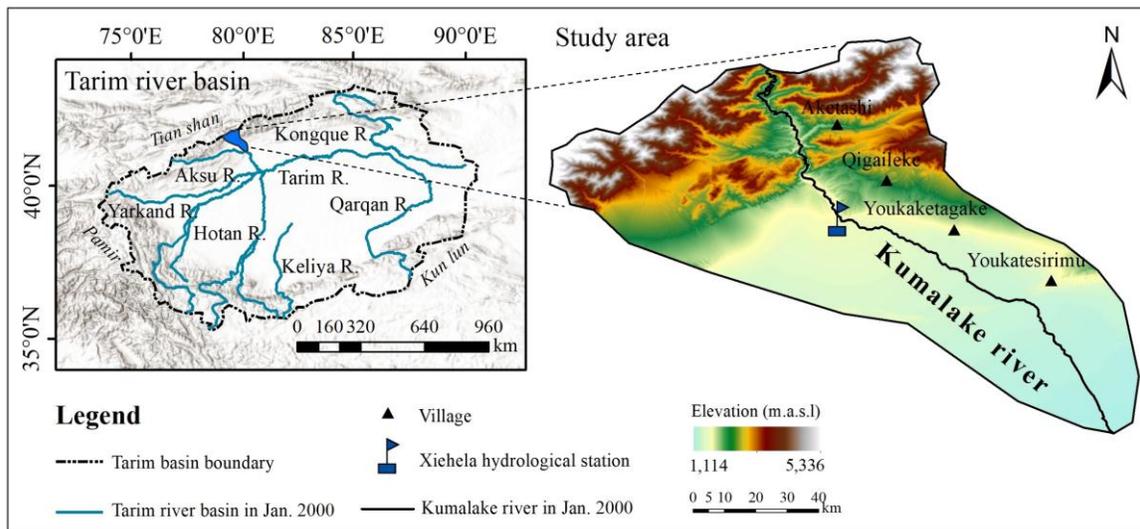
310

311   **Figure 4.** Schematic diagram of the watershed in the study area. Basemap: Esri World

312   Hillshade (Esri).

313

3.2 Model input data

In this study, LE-PIHM combined with a river channel extraction technique is employed to simulate the spatial distribution of river channels. Notably, four categories of physical properties within the study area, i.e., soil, aquifer, bedrock, and land cover, exhibit significant spatial heterogeneity (see Table 1 and Fig. 5). The driving force data in LE-PIHM primarily include leaf area index, precipitation rate, air temperature, downward shortwave radiation, snowmelt rate, wind speed, and relative humidity (Table 1)
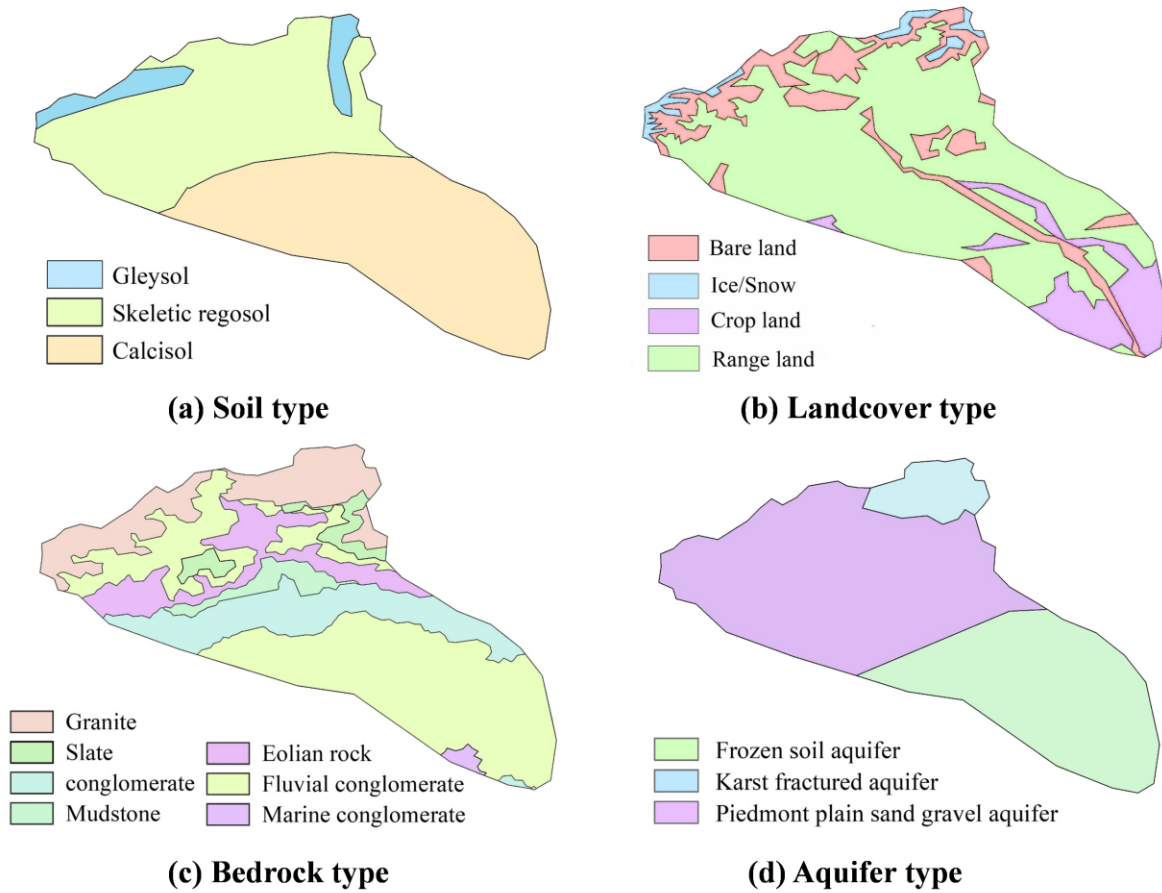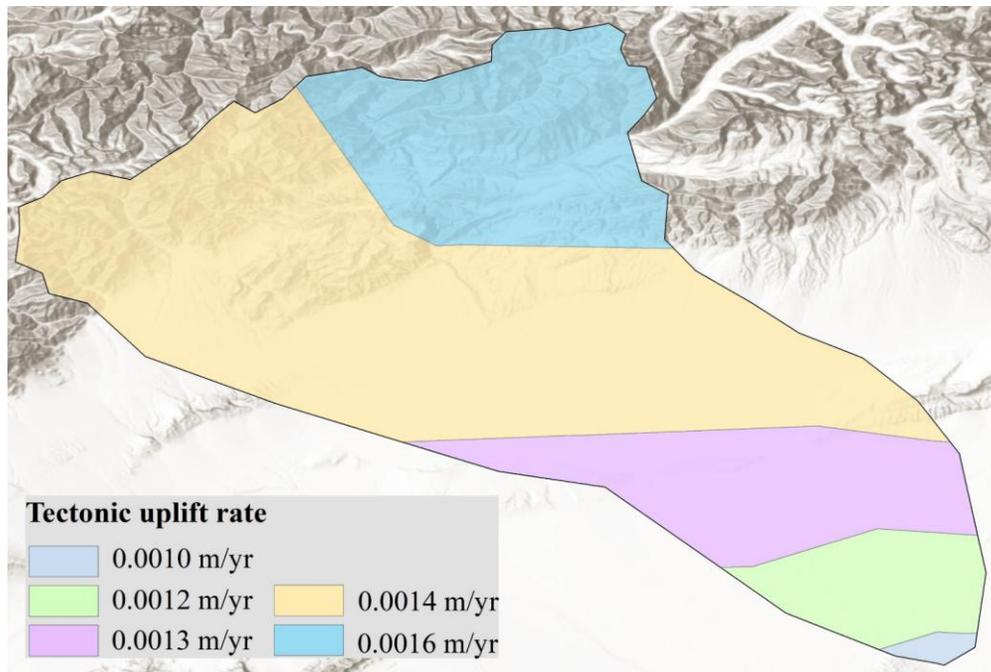

Figure 5. Zonation of average tectonic uplift rates in the study area from 2000 to 2021.

323   **Table 1.** Types and sources of input data for the landscape evolution model.

Data Type	Spatial Resolution	Temporal Resolution	Data Source	URL
Soil type	1:5000000	/	Food and Agriculture Organization of the UN	https://data.apps.fao.org/?lang=en
Bedrock type	1:1000000	/	International Soil Reference and Information Center	https://soilgrids.org/
Land cover	10 m	/	Environmental Systems Research Institute, Inc	https://livingatlas.arcgis.com/landcover/
Aquifer type	/	/	China Cartographic Publishing House	https://www.sinomaps.com/pub/
Leaf area index	0.5°×0.625°	1h		
Surface roughness	0.5°×0.625°	1h		
Precipitation rate	0.25°	3h		
Air temperature	0.25°	3h		
Shortwave radiation	0.25°	3h		
Canopy interception storage	0.25°	3h	National Aeronautics and Space Administration	https://www.nasa.gov/
Soil water storage	0.25°	3h		
Snow depth	0.25°	3h		
Snow melt rate	0.25°	3h		
Wind speed	0.25°	3h		
Relative humidity	1.25°	3h		
Initial surface elevation	30 m	/		
Initial bedrock depth	250 m	/	International Soil Reference and Information Center	https://isric.org/

All links in the table were last accessed on 2 December 2025

324

As an essential driving factor in landscape evolution, the rock uplift rate data were derived from the vertical crustal velocity field of China (Wang et al., 2020; Zubovich et al., 2016), with the Chinese GNSS velocity field taken from Wang and Shen (2020; https://doi.org/10.7910/DVN/C1WE3N) and the Pamir–Tien Shan GNSS velocities from Zubovich et al. (2016; https://doi.org/10.1002/2015TC004055). The spatial distribution of the average rock uplift rate in the study area from 2000 to 2021 was obtained through kriging interpolation (Fig. 6).

**Figure 6.** Zonation of average tectonic uplift rates in the study area from 2000 to 2021. Basemap: Esri World Hillshade (Esri).

3.3 Observed river channel planform data

Observed river channel planform data for December 2007, February 2014, and December 2021 were obtained using the Google Earth Pro image platform (see Fig. 7). Among these, the spatial distribution of river channels from December 2007 and February 2014 were used to identify the posterior distribution of model parameters (i.e., key

340   parameters of LE-PIHM), while the December 2021 data were employed to validate the

341   river channel migration results.

342
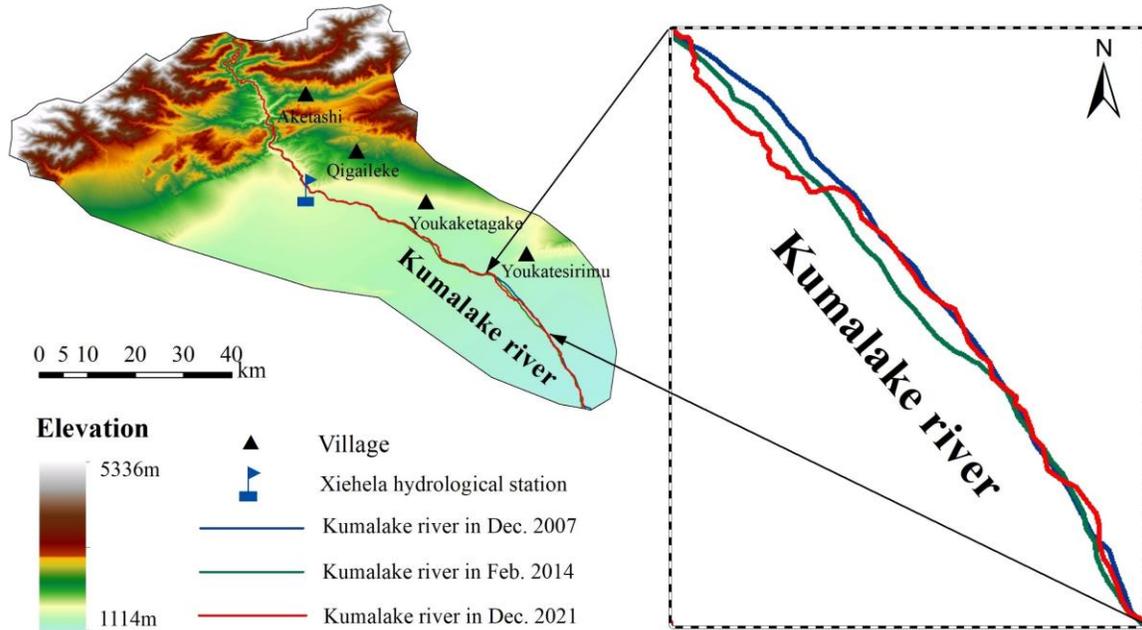
343   **Figure 7.** The spatial distribution of the Kumalake River channels in the study area.

3.4 Model settings

345   The outlet of the Kumalake River Basin was set at the intersection with the

346   southeastern boundary of the study area, while all other boundaries were defined as no-

347   flow boundaries. An unstructured triangular mesh was used to discretize the study area

348   spatially. To accurately capture the landscape evolution processes in areas surrounding the

349   river channel, mesh refinement was applied in the channel zones, with grid sizes less than

350   50 meters near the river. A total of 25,968 unstructured triangular elements were generated

351   for the study area (see Fig. 8a).
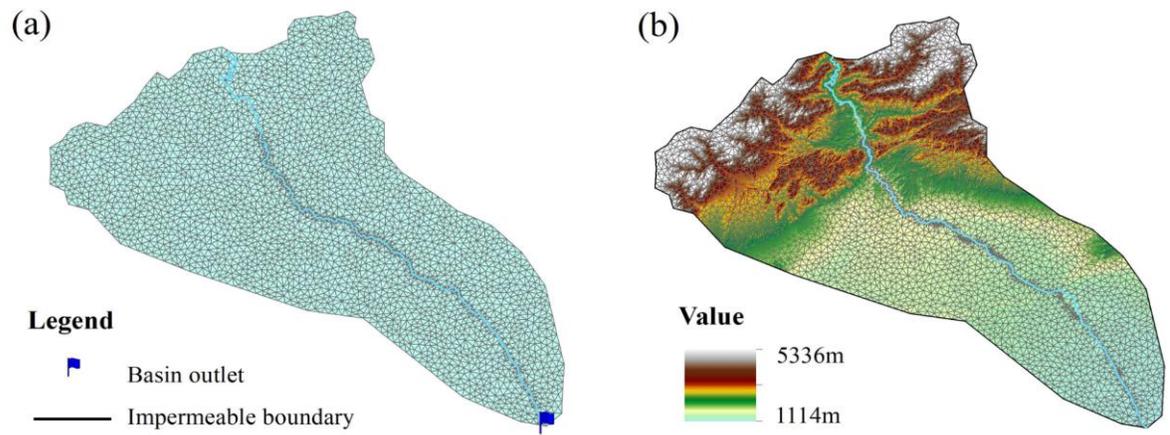
Figure 8. Mesh discretization and initial elevation grid of the research area.

The initial conditions required by LE-PIHM include ground surface elevation (Fig. 8b), canopy interception storage, snow depth, surface water depth, soil water storage, and groundwater storage. The canopy interception storage is initialized to 0 m in the model (Fig. 9 and Table 1).

The model was configured to run from January 2000 to December 2021, covering a total of 264 months (22 years). To capture the seasonal variability of hydrologic processes in the study area while controlling computational load, the time step was set to one month. The LE-PIHM model was executed on an Intel Xeon E5-2680 v3 server, with an average runtime per simulation of 195 minutes.
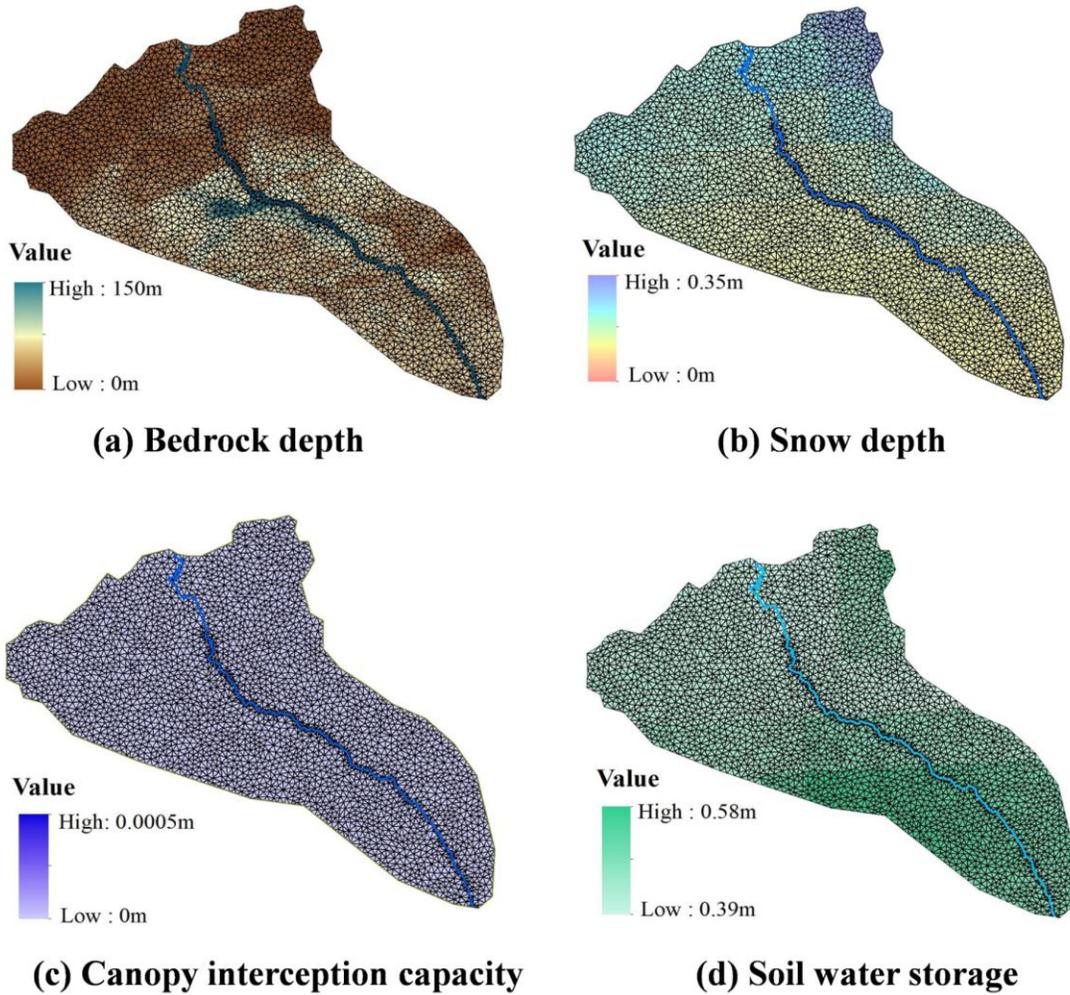
Figure 9. The initial conditions of landscape evolution model.

3.5 LSTM-based surrogate model for uncertainty analysis

After constructing the basin-scale channel migration model, the next part is to conduct parameter uncertainty analysis, followed by the reconstruction of river channel migration over 2000–2021 and the prediction of landscape evolution and river channel changes from 2021 to 2100 under future climate scenarios.

However, performing parameter uncertainty analysis using MCMC requires a large number of runs of the original model (i.e., the basin-scale channel migration model), which results in a significant computational burden. To reduce this computational cost, this study

373 employs an LSTM network to construct a surrogate model for river channel migration. The

374 surrogate model employs a two-layer LSTM architecture followed by a linear fully

375 connected layer, with normalized LE-PIHM parameters as inputs and flattened planar

376 river-channel coordinates as outputs, and is trained using the Adam optimizer to minimize

377 the root-mean-square error (RMSE) loss between predicted and reference channel

378 planforms. The main steps and more details of LSTM-based surrogated models are as

379 follows:

380 *i*. The Sobol method is applied for parameter sensitivity analysis. Considering the

381 property parameters of surface cover, soil, aquifer, and bedrock, 11 highly sensitive

382 parameters LE-PIHM are selected as the input variables for the surrogate model (Table 2).

383 **Table 2.** The parameters of landscape evolution model and their prior ranges.

Parameters	Units	Prior distribution
Vegetation fractional coverage (VegFrac)	/	[0.075, 0.225]
Root zone depth (Rzd)	m	[0.15, 0.45]
Soil vertical hydraulic conductivity (KVs)	m/d	[0.30, 0.90]
Soil porosity (Ns)	/	[0.175, 0.525]
Morphological diffusivity (K1)	m^2/yr	[0.10, 0.30]
Soil particle diameter (Ds)	m	[0.0005, 0.0015]
Aquifer horizontal hydraulic conductivity (KHg)	m/d	[3.50, 10.50]
Aquifer vertical hydraulic conductivity (KVg)	m/d	[0.70, 2.10]
Bedrock weathering rate for bare rock (P0)	m/yr	[0.004, 0.012]
Tectonic uplift rate (U)	m/yr	[0.00050, 0.00155]
Coefficient for bedrock weathering equation (α)	1/m	[0.01, 0.03]

384 *ii*. Latin hypercube sampling is employed to generate 3,000 sample sets within the

385 prior ranges of the input variables.

386 *iii*. These 3,000 parameter sets are individually input into the LE-PIHM model to

387 generate surface elevation data at three time points, December 2007, February 2014, and

388 December 2021. Subsequently, the corresponding spatial distribution of river channel is

389 extracted through Arcpy scripting in ArcGIS. For each parameter set, the corresponding

390   river channel is discretized uniformly into 2,000 points, producing 2,000 sets of planar

391   coordinates of reaches.

392   *iv*. The obtained 3,000 sets of input variables and their corresponding coordinates are

393   split into training and validation datasets at 70% and 30% ratios. The LSTM network is

394   trained to learn the nonlinear mapping between the input variables and river channel

395   positions, thereby constructing a surrogate model for river channel migration. The network

396   terminates in a fully connected output layer with a linear activation function and He-normal

397   weight initialization. Training is performed using the Adam optimizer with a learning rate

398   of 1×10^{-3}, minimizing the root-mean-square error (RMSE) between the predicted and

399   reference river coordinate points. The model is trained for 10,000 epochs with a batch size

400   of 100 and a validation split of 0.1.

401   As shown in the validation results (Table 3), the surrogate model constructed using

402   LSTM demonstrates great predictive performance for river channel locations (i.e., the

403   planar coordinates of river reaches). It achieved a mean absolute error (MAE) of 1,411.16

404   m, a root mean square error (RMSE) of 1,980.10 m, and a coefficient of determination (R^2)

405   of 0.983. Furthermore, the average Hausdorff distance of the entire river between the

406   surrogate model and original model outputs is 229.71 m. Given the total length of river

407   channels in the study area is 89,337.95 m, this corresponds to only 0.25%. Thus, these

408   results demonstrate that the surrogate model for basin-scale river channel migration

409   exhibits high accuracy and reliability and can replace the original model for river channel

410   dynamics simulation.

411   **Table 3.** Evaluations of the surrogate model for basin-scale river channel migration.

Metrics	RMSE	MSE	R^2	H/Total length of river
Results	1411.60m	1980.10m	0.98	0.0025

412   The spatial distribution of river channels predicted by the original model and the

413 surrogate model are compared across three time points (Fig. 10). The surrogate model

414 closely matches the original in the middle and upper reaches of the river channel, while

415 some deviations occur in the downstream reaches. This discrepancy is primarily due to the

416 mountainous topography upstream, where the landscape is rugged and river channels are

417 relatively stable. In contrast, the downstream region is a flat plain, where river channel

418 migration is highly sensitive to model parameters, leading to slightly reduced accuracy in

419 the surrogate model's performance in that area.

420   Compared to the original model, the surrogate model for basin-scale river channel

421 migration achieves approximately a 20,000-fold increase in computational speed.

422 Therefore, employing this surrogate model in the parameter uncertainty analysis of river

423 channel migration can significantly reduce computational costs and effectively alleviate

424 the computational burden associated with the uncertainty analysis process.

425
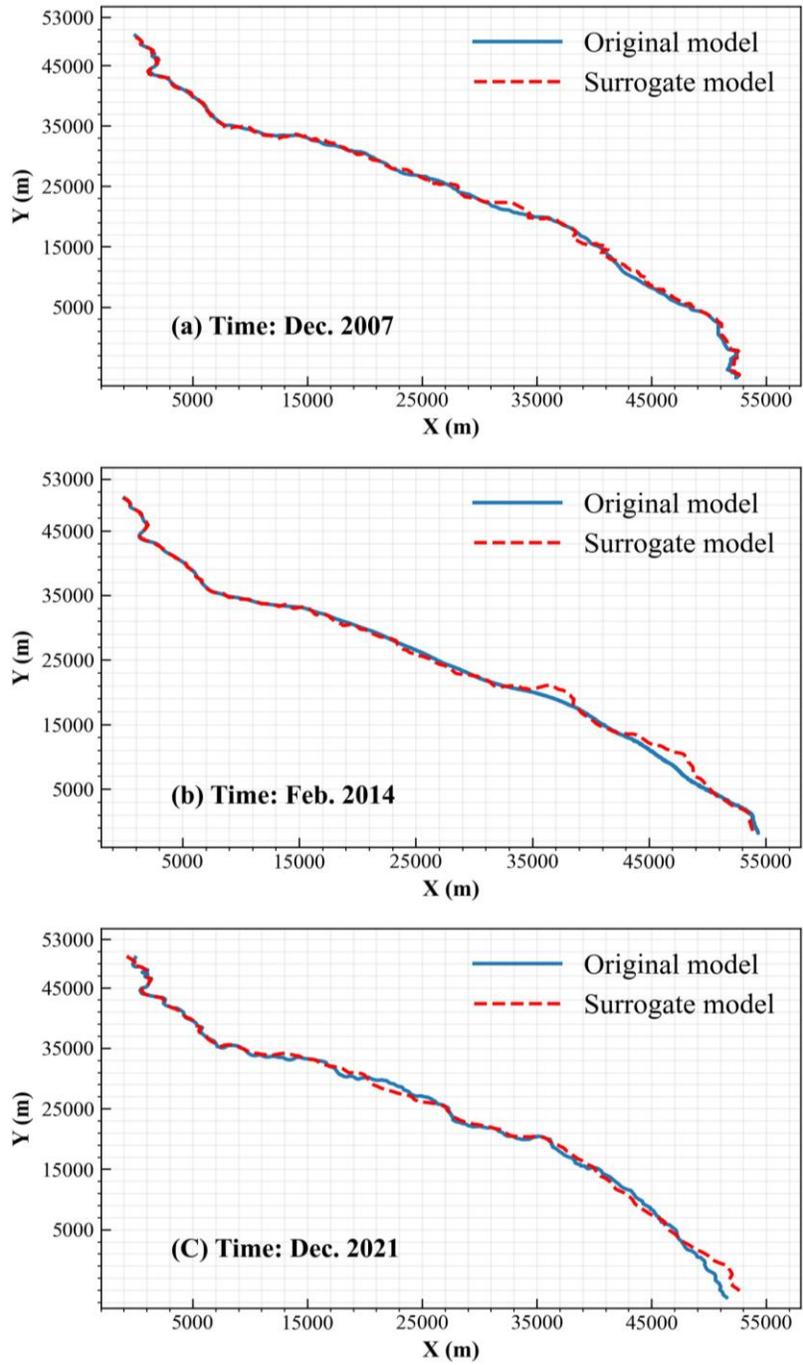
Figure 10. Comparison between the original river channel migration model and the

surrogate model at different time points.

4. Results and discussion

4.1 Parameter uncertainty analysis

4.1.1 MCMC configuration

431

432   The river channel migration model includes 11 unknown parameters to be identified,

433   with their prior distributions assumed to be uniform within the specified range (Table 2).

434   The MCMC simulation is performed using the DREAMzs sampling algorithm, with three

435   parallel Markov chains. Both the burn-in and formal sampling stages consist of 2,000

436   iterations. Additionally, the evolution of the Markov chains employs the modified

437   likelihood function described in Sect. 2.3.2. Based on the inferred posterior distributions

438   of the parameters, the posterior distribution of the river channel is obtained.

4.1.2 Posterior distributions of model parameters

439

440   The posterior probability density histograms of the river channel migration model

441   parameters through MCMC (horizontal axis indicates the corresponding prior ranges; Fig.

442   11), together with the maximum likelihood parameter set (Table 4). It is easy to find that

443   several parameters, such as the vertical soil hydraulic conductivity (KVs), hillslope

444   diffusion coefficient (K1), bare-bedrock weathering rate (P0), soil grain size (Ds), and

445   vegetation fraction (VegFrac) exhibit clear convergence to relatively narrow and

446   concentrated posterior ranges after calibration. This suggests that channel-planform

447   predictions are highly sensitive to these parameters, and that they exert strong control on

448   basin-scale erosion-deposition balance and channel migration behavior.

449   In contrast, the posterior distributions of some parameters, such as aquifer horizontal

450   hydraulic conductivity (KHg), the weathering-law coefficient (α), and the tectonic uplift

451   rate (U), remain comparatively broad. This indicates that, given the spatial scale of this

452   study and the available observational constraints, channel-planform position is less

453   responsive to these parameters. Over the past 22 years, channel migration in the basin scale

454　may have limited sensitivity to tectonic uplift, or the effects of uplift may be partially

455　compensated by other parameters within the coupled hydro-geomorphic system.
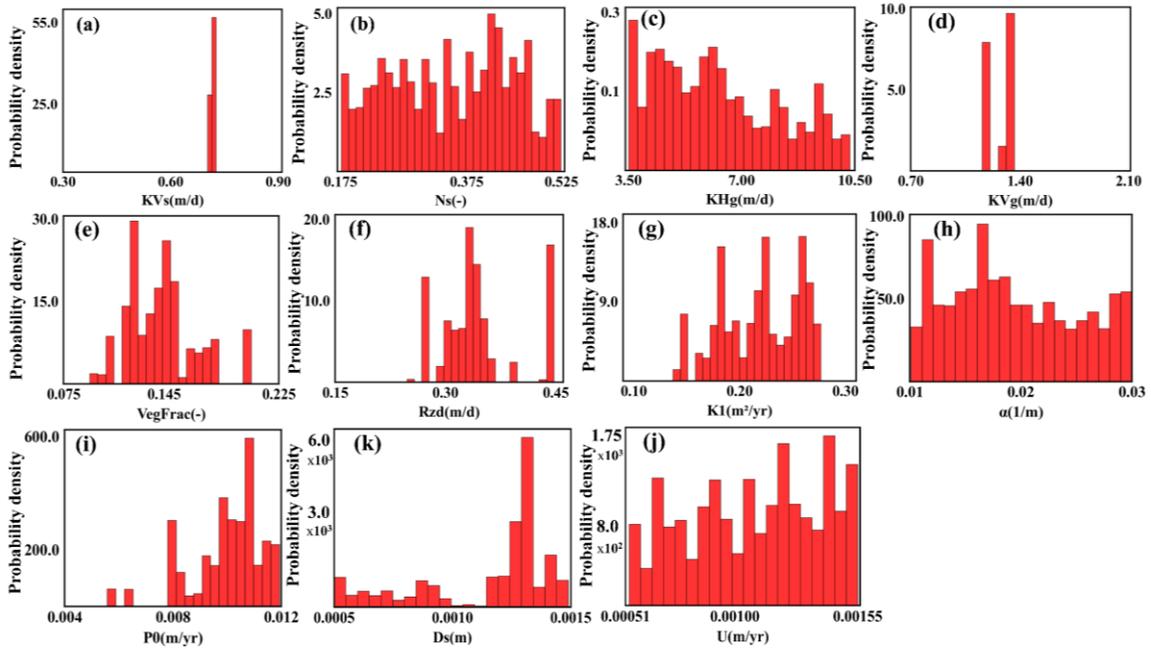
456

457　**Figure 11.** Calibrated posterior distributions of model parameters.

458　**Table 4.** Parameter set corresponding to the maximum likelihood estimate.

Parameters	Units	Parameter value
Vegetation fractional coverage (VegFrac)	/	0.14
Root zone depth (Rzd)	m	0.17
Soil vertical hydraulic conductivity (KVs)	m/d	0.43
Soil porosity (Ns)	/	0.24
Morphological diffusivity (K1)	m^2/yr	0.20
Soil particle diameter (Ds)	m	0.001
Aquifer horizontal hydraulic conductivity (KHg)	m/d	9.60
Aquifer vertical hydraulic conductivity (KVg)	m/d	1.90
Bedrock weathering rate for bare rock (P0)	m/yr	0.007
Tectonic uplift rate (U)	m/yr	0.0008
Coefficient for bedrock weathering equation (α)	1/m	0.02

459

4.1.3 Reconstruction of river channel migration (2000-2021)

460

461   Based on the posterior distributions of the identified parameters, the river channel

462   evolution from 2000 to 2021 in the study area was reconstructed. The result shows that the

463   predicted confidence interval fully encompasses the observed river channel (Fig. 12), and

464   the blue shaded region denotes the 95% confidence interval, the red line represents the

465   observed river channel in Fig. 12. The average Hausdorff distance of the entire river

466   between the simulated channel (marked in black line in Fig. 12) with the maximum

467   likelihood parameter set and the observed channel is 225.42 m, which accounts for only

468   0.25% of the total river channel length. This indicates that the discrepancy between the

469   simulated and observed river channel per unit length is minimal, demonstrating the high

470   accuracy of the calibrated river channel migration model. Therefore, the river channel

471   model facilitated by Bayesian parameter uncertainty quantification can reliably predict the

472   river channel migration processes within the study area.
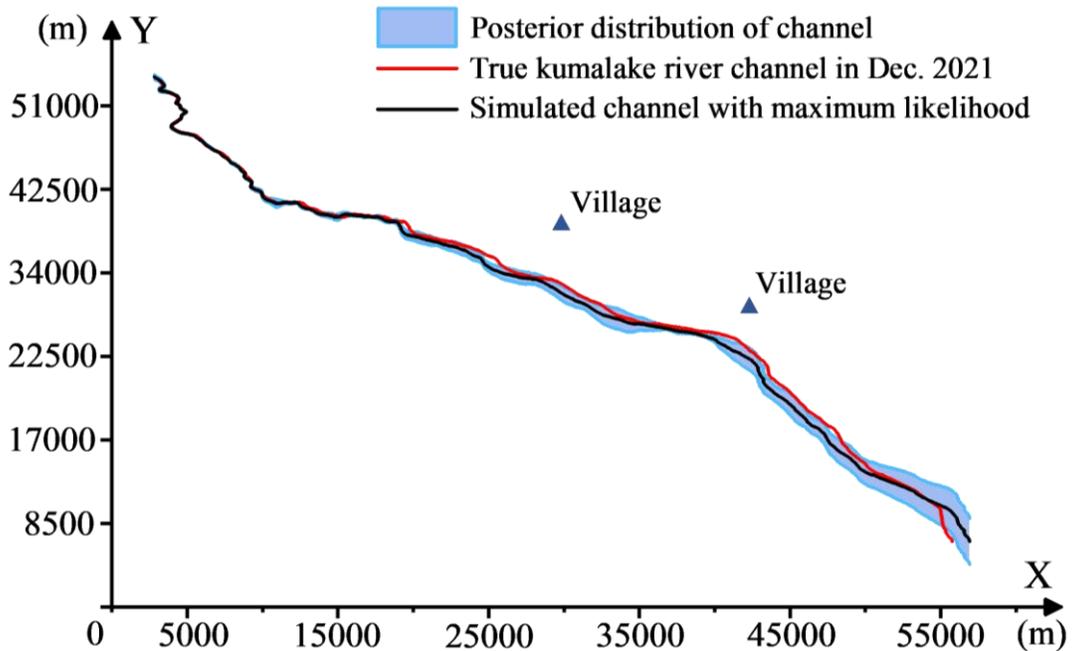
473

474   **Figure 12.** The predicted Kumalake River channel at December 2021.

475   Remote sensing images (Fig. 13) collected during the simulation period of the study

476   area indicates that, beginning in 2012, the villages along the river initiated to develop

477   cultivated land near the river channel. This anthropogenic activity altered key parameters

478   related to land cover and soil type, and may have been a driving factor for the gradual

479   southward migration of local river reaches. However, this mechanism of human-induced

480   change is not explicitly represented in the landscape evolution model, which may partly

481   explain the reduced simulation accuracy in the downstream region. Nevertheless, the

482   parameter uncertainty analysis conducted in this study helps to partially compensate for

483   the effects of land reclamation, keeping the prediction deviation of basin-scale river

484   channel migration model within an acceptable range.
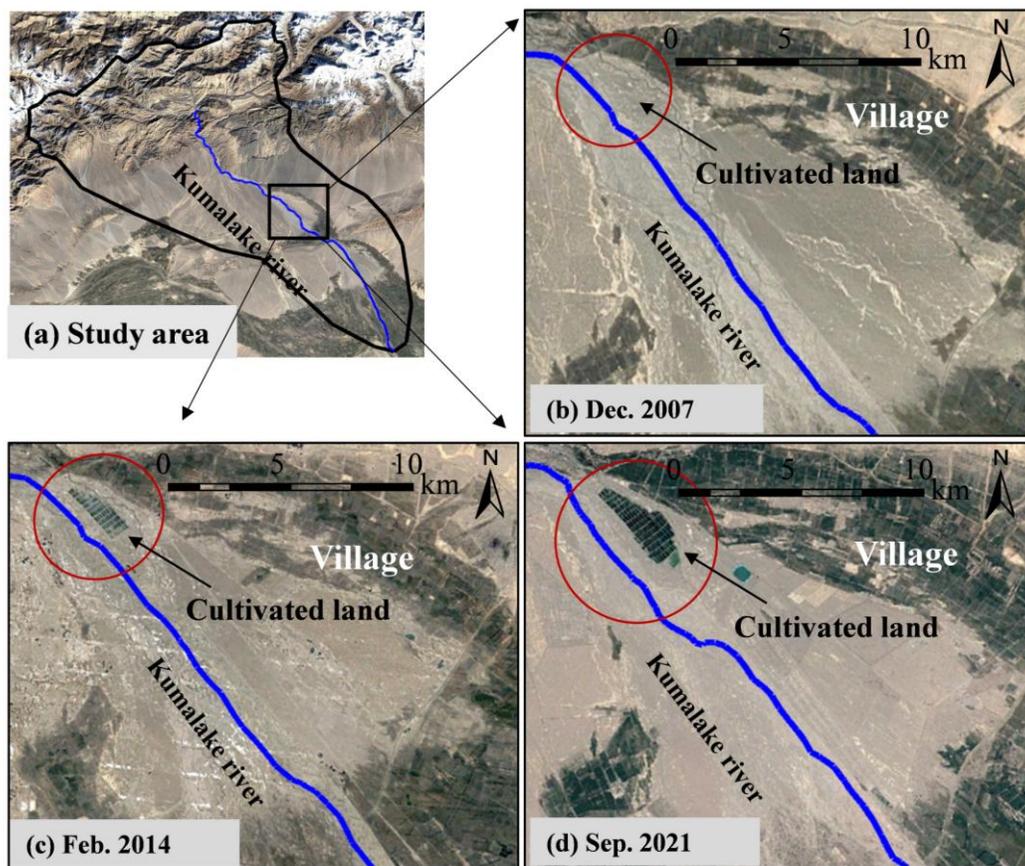
485

486   **Figure 13.** Formation process of cultivated land along the river in the study area. Satellite

487   imagery: © Google Earth 2007, 2014, 2021, modified by the authors.

4.2 Prediction of river channel migration in future (2021-2100)

Future climate change will influence landscape evolution and river channel migration, thereby affecting regional water resource patterns and ecological environments. The EC-Earth3-Veg climate model, released under phase 6 of the Coupled Model Intercomparison Project (CMIP6), incorporates vegetation-climate interactions and is well-suited for evaluating terrestrial ecosystem and hydrological responses under different climate scenarios (Alsalal et al., 2024; Eyring et al., 2016). Based on the EC-Earth3-Veg model, this study adopts four scenarios of shared socioeconomic pathways (SSPs), i.e., SSP1-2.6, SSP2-4.5, SSP3-7.0, and SSP5-8.5. Each of the four climate scenarios reflects a distinct pathway of global socioeconomic development and associated impacts on greenhouse gas emissions and climate change (O'Neill et al., 2016).

The scenario forcing fields are mapped to the LE-PIHM basin computational units using bilinear interpolation. To maintain consistency with the monthly time step adopted in LE-PIHM, the forcing data are temporally aggregated to monthly resolution prior to being used as model inputs. Scenario-based simulations of landscape evolution and river channel migration were conducted by using these climate conditions as the driving force of LE-PIHM. The climate conditions for these scenarios over the period (2021–2100) are characterized by the annual mean temperature and precipitation (Table 5 and Fig. 14).

Table 5. Statistics of four climate scenarios under the EC-Earth3-Veg model.

| Climate model	Average precipitation	Average temperature	Shared Socioeconomic Pathways
	284.97mm	3.76°C	SSP-1.26
EC-Earth3-Veg	300.89mm	4.05°C	SSP-2.45
	301.76mm	4.68°C	SSP-3.70
	310.16mm	5.33°C	SSP-5.85
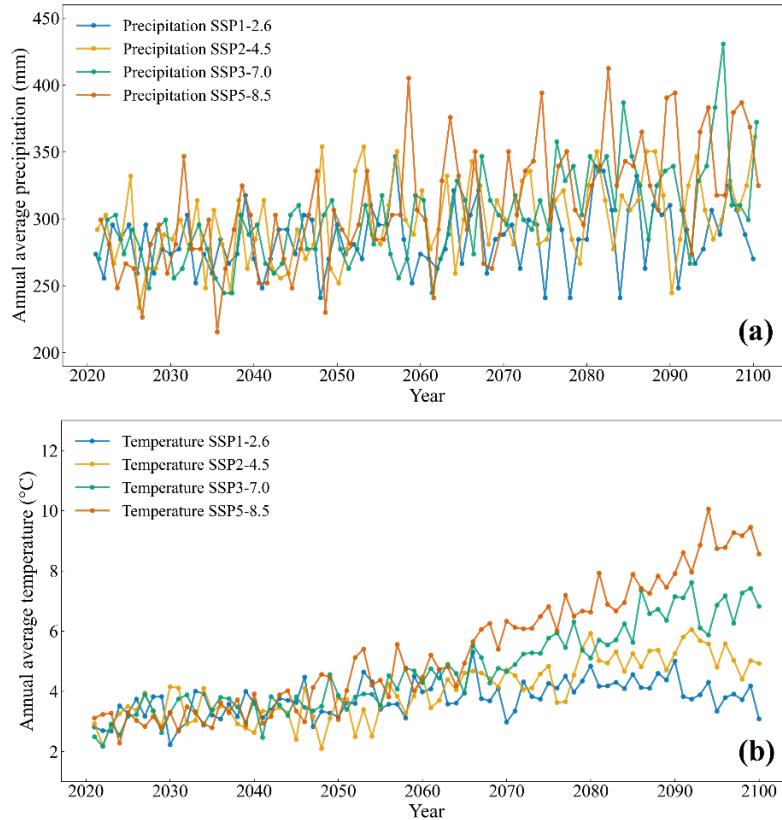
Figure 14. Annual mean precipitation and temperature for the four climate scenarios.

Using LE-PIHM and the parameter set corresponding to the maximum likelihood estimate (Table 4), the landscape evolution and river channel migration from 2021 to 2100 were simulated for the study area under four climate change scenarios. After 80 years of simulated landscape evolution, the overall topographic pattern of the region remains characterized by higher elevations in the north and lower elevations in the south, with elevation changes ranging from +1.39 m to -0.37 m. The simulation results under the four EC-Earth3-Veg climate scenarios demonstrate that the elevation change and river channel migration in basin scale by the year 2100 exhibit distinct characteristics (Fig. 15 a). In the northern mountainous area, distinct alternating patterns of uplift and subsidence are observed, with relatively large magnitudes of change. This is primarily due to intense bedrock weathering and steep slopes in the mountains, where the regolith layer is thin and

the weathered soil and sediment are prone to downslope transport into adjacent low-lying

regions, resulting in significant elevation fluctuations. In contrast, the southern plain

exhibits gentle topography and minimal elevation differences, making it less conducive to

large-scale sediment transport. As a result, the landscape undulation in the plain is

relatively mild and limited in amplitude.
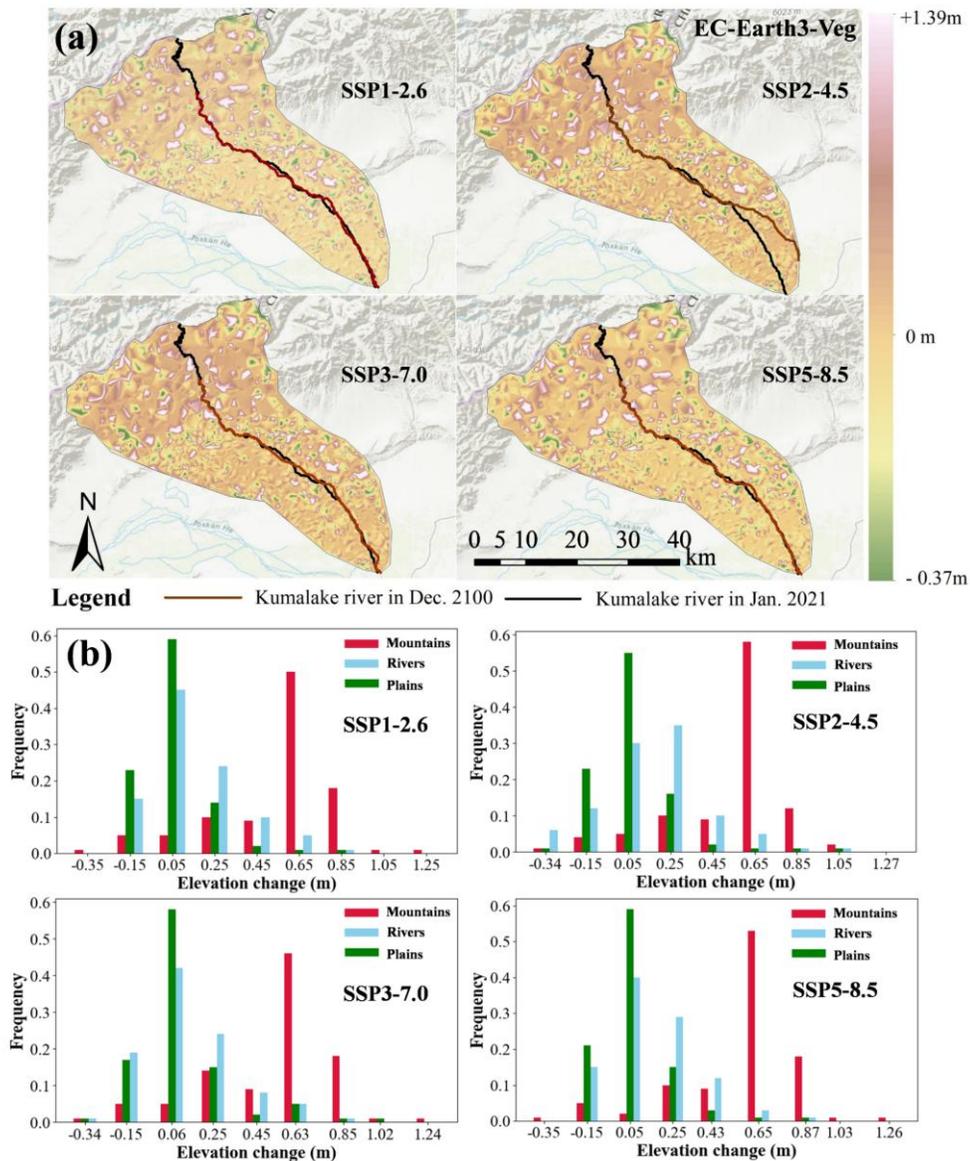
Figure 15. Spatial distribution of river channel (a) and Elevation change (b) under four

future climate scenarios based on the EC-Earth3-Veg climate model. Basemap: Esri World

Hillshade (Esri).

529   Under the EC-Earth3-Veg climate model, the four future climate scenarios induce

530   distinct patterns of river channel migration. By the end of the simulation period (2100), the

531   upstream reaches of the Kumalake River remain largely unchanged from their 2021

532   positions. This stability is attributed to the fact that these reaches flow through narrow and

533   geomorphologically stable canyon landscape, where external disturbances are minimal and

534   the river alignment and morphology remain relatively constant. In contrast, several

535   downstream reaches situated in the plain exhibit varying degrees of northward migration.

536   This phenomenon is mainly driven by the relatively gentle topography of the plains,

537   increased sediment deposition, redistribution of flow energy, and anthropogenic activities.

538   These factors collectively lead to channel swinging, incision, or aggradation, gradually

539   shifting the river channel position.

540   The four scenarios under EC-Earth3-Veg exhibit significant differences in

541   temperature and precipitation characteristics, as well as in the extent of river channel

542   migration (Table 6). Notably, under the SSP2-4.5 scenario, although the climate variability

543   is not the most intense among the scenarios, the elevation change shows the largest

544   amplitude, and the topographic changes in the river area are more pronounced (Fig. 15 a),

545   leading to a shift of the downstream river channels into the plain area. This suggests that

546   the climate changes in this scenario trigger a sudden and intense spatial reorganization of

547   the river network, resulting in significant morphological transformation. The specific

548   combination of climatic conditions may cause the river system to approach an evolutionary

549   threshold (Church et al., 2002; Meyer et al., 2018). When such a critical threshold is

550   reached, the river system may undergo abrupt transitions, manifesting as regime shifts

551   (Church et al., 2002).

552   In summary, within the LE-PIHM landscape evolution framework, channel planform

553   dynamics and elevation changes are jointly controlled by the following processes. (*i*)

554   Precipitation-runoff mechanisms, including rainfall, infiltration and runoff generation, and

555   surface-groundwater exchange; (*ii*) Sediment supply and transport capacity, including

556   hillslope diffusion, weathering-driven sediment production, and river sediment transport;

557   (*iii*) Landscape-flow-routing feedbacks, whereby landscape evolution and the associated

558   adjustment of D8-based flow paths modify local slope and discharge concentration.

559   These results indicate that the process of river channel migration in the study area

560   under climate forcing varies across scenarios. Future climate conditions play a critical role

561   in regional landscape evolution and river dynamics. Furthermore, the complex feedbacks

562   between climate change and geomorphic systems highlight the importance of incorporating

563   these interactions in predictive modeling of fluvial landscape evolution and watershed

564   management planning.

565   **Table 6.** Statistics of climate scenarios and average Hausdorff distance of river migration.

	SSP1-2.6	SSP2-4.5	SSP3-7.0	SSP5-8.5
Variance of precipitation (mm^2)	576	922.45	1227.62	1942.72
Range of precipitation (mm)	105.85	127.75	186.15	197.1
Variance of temperature ($°C^2$)	0.34	0.92	1.99	4.27
Range of temperature (°C)	3.08	3.96	5.45	7.79
H(m)	333.26	1873.37	405.69	304.85

566 # **5. Conclusions**

567   River channel migration at the basin scale not only determines the spatial distribution

568   pattern of regional river networks, but also exerts profound influences on local ecosystems

569   and the development of civilizations within the basin. Simulating river channel migration

570   at the basin scale aids in quantitatively reconstructing this long-term, complex dynamic

571   processes and also provides a scientific basis for decision-making in response to climate

572   change and natural disasters. To address the limitations of traditional river channel

573   migration models in temporal and spatial scale applications, this study integrates a

574   landscape evolution model with river channel extraction techniques, achieving accurate

575   and reliable simulation of river channel migration processes at the basin scale. Using the

576   Kumalake River Basin as a case study, the river channel migration process in the region is

577   reconstructed based on the LE-PIHM landscape evolution model and river channel

578   extraction techniques. The main conclusions of this study are as follows:

579   1. The LSTM-based surrogate model for river channel migration demonstrates high

580   accuracy and effectively overcomes the computational challenge associated with parameter

581   uncertainty analysis. The parameter calibration using MCMC requires numerous

582   executions of the LE-PIHM model and river channel extraction, resulting in prohibitive

583   computational demands. The surrogate model for basin-scale river channel migration based

584   on LSTM networks accurately characterizes the response relationship between landscape

585   evolution parameters and river channel locations, effectively solving the problem of

586   computational burden in Bayesian uncertainty analysis.

587   2. The river channel migration model facilitated by Bayesian parameter uncertainty

588   quantification can reliably predict the river channel evolution process within the study area.

589   Based on the inferred posterior distributions of model parameters, the predicted confidence

590   interval of the channel fully encompasses the actual river location. The average Hausdorff

591   distance between the simulated river channel with the maximum likelihood parameter set

592   and the observed river channel is 225.42 m, which accounts for only 0.25% of the total

593   channel length. Thus, the basin-scale river channel migration model incorporating

Bayesian uncertainty analysis demonstrates high reliability and predictive capability, enabling effective characterization of river migration processes within the study area.

3. River channel evolution under different climate scenarios demonstrates significant variability, and future climate change will profoundly affect basin geomorphological characteristics and river network configurations. Based on the EC-Earth3-Veg model released by CMIP6, the landscape evolution and river channel migration in the study area from 2021 to 2100 were projected under four Shared Socioeconomic Pathways (SSP1-2.6, SSP2-4.5, SSP3-7.0, and SSP5-8.5). The results indicate that climate change and geomorphological systems exhibit complex response mechanisms.

Author contributions.

JW and XZ conceptualized the study and designed the research methodology. JW and QW conducted the simulations and implemented the methodology. JW produced all the figures and tables. XZ and JW contributed to the data validation and data curation. DW and JW supervised the research. All authors reviewed, edited and approved the final version of the manuscript.

Competing interest.

The contact author has declared that none of the authors has any competing interests.

Data Availability.

The temperature and precipitation data used in this study from the World Data Center for Climate (WDCC) are open-access and publicly available: EC-Earth-Consortium EC-Earth3-Veg (https://doi.org/10.26050/WDCC/AR6.C6CMEEEVE, CMIP6). The observed river channel planform data used for uncertainty analysis mentioned in Sect. 3.3 have been made publicly available via the Hydroshare platform (https://doi.org/10.4211/hs.a6eb2a2c8ae746cf99d5d89a5ed2600b, Zeng and Wu., 2025).

References

Ali, M. S., Hasan, M. M., and Haque, M.: Two-dimensional simulation of flows in an open channel with groin-like structures by iRIC Nays2DH, Math. Probl. Eng., 2017, 1275498, https://doi.org/10.1155/2017/1275498, 2017.

Alsalal, S., Tan, M. L., Samat, N., Al-Bakri, J. T., and Zhang, F.: Temperature and precipitation changes under CMIP6 projections in the Mujib Basin, Jordan, Theor. Appl. Climatol., 155, 7703–7720, https://doi.org/10.1007/s00704-024-05087-2, 2024.

Barnhart, K. R., Hutton, E. W. H., Tucker, G. E., Gasparini, N. M., Istanbulluoglu, E., Hobley, D. E. J., Lyons, N. J., Mouchene, M., Nudurupati, S. S., Adams, J. M., and Bandaragoda, C.: Short communication: Landlab v2.0: a software package for Earth surface dynamics, Earth Surf. Dynam., 8, 379–397, https://doi.org/10.5194/esurf-8-379-2020, 2020.

Bishop, P.: Long-term landscape evolution: linking tectonics and surface processes, Earth Surf. Process. Landf., 32, 329–365, https://doi.org/10.1002/esp.1493, 2007.

Bogoya, J. M., Cuate, O., & Vargas, A. (2019). The Averaged Hausdorff Distances in Multi-Objective Optimization: A Review. Mathematics

Braun, J. and Sambridge, M.: Modeling landscape evolution on geological time scales: a new method based on irregular spatial discretization, Basin Res., 9, 27–52, https://doi.org/10.1046/j.1365-2117.1997.00030.x, 1997.

Church, M.: Geomorphic thresholds in riverine landscapes, Freshw. Biol., 47, 541–557, https://doi.org/10.1046/j.1365-2427.2002.00919.x, 2002.

Coulthard, T. J., Neal, J. C., Bates, P. D., Ramirez, J., de Almeida, G. A., and Hancock, G. R.: Integrating the LISFLOOD-FP 2D hydrodynamic model with the CAESAR model: implications for modelling landscape evolution, Earth Surf. Process. Landf., 38, 1897–1906, https://doi.org/10.1002/esp.3478, 2013.

Desormeaux, C., Godard, V., Lague, D., Duclaux, G., Fleury, J., Benedetti, L., Bellier, O., and the ASTER Team: Investigation of stochastic-threshold incision models across a climatic and morphological gradient, Earth Surf. Dynam., 10, 473–492, https://doi.org/10.5194/esurf-10-473-2022, 2022.

ESRI: ArcGIS Pro, Esri, available at: https://www.esri.com/en-us/legal/requirements/open-source-acknowledgements, last access: 6 December 2023, 2022.

Eyring, V., Bony, S., Meehl, G. A., Senior, C. A., Stevens, B., Stouffer, R. J., and Taylor, K. E.: Overview of the Coupled Model Intercomparison Project Phase 6 (CMIP6) experimental design and organization, Geosci. Model Dev., 9, 1937–1958, https://doi.org/10.5194/gmd-9-1937-2016, 2016.

Goren, L., Willett, S. D., Herman, F., and Braun, J.: Coupled numerical–analytical approach to landscape evolution modeling, Earth Surf. Process. Landf., 39, 522–545, https://doi.org/10.1002/esp.3514, 2014.

Graves, A. and Schmidhuber, J.: Framewise phoneme classification with bidirectional LSTM and other neural network architectures, Neural Netw., 18, 602–610, https://doi.org/10.1016/j.neunet.2005.06.042, 2005.

Hickin, E. J.: River channel changes: retrospect and prospect, in: Modern and ancient fluvial systems, 59–83, https://doi.org/10.1002/9781444303773.ch5, 1983.

Hochreiter, S. and Schmidhuber, J.: Long short-term memory, Neural Comput., 9, 1735–1780, https://doi.org/10.1162/neco.1997.9.8.1735, 1997.

Hou, R., Zeng, X., Wang, D., and Wu, J.: Evaluating spatial downscaling surrogate models for landscape evolution simulations in the Tarim River basin, China, Stoch. Environ. Res. Risk Assess., 39, 2479–2496, https://doi.org/10.1007/s00477-025-02980-8, 2025.

Hritz, C.: Tracing settlement patterns and channel systems in southern Mesopotamia using remote sensing, J. Field Archaeol., 35, 184–203, https://doi.org/10.1179/009346910X12707321520477, 2010.

Hsu, S. Y. and Hsu, S. M.: Morphological evolution mechanism of gravel-bed braided river by numerical simulation on Da-Jia River, J. Hydrol., 613, 128222, https://doi.org/10.1016/j.jhydrol.2022.128222, 2022.

Ikeda, S., Parker, G., and Sawai, K.: Bend theory of river meanders, Part 1: Linear development, J. Fluid Mech., 112, 363–377, https://doi.org/10.1017/S0022112081000451, 1981.

Lei, T. L. and Lei, Z.: Harmonizing full and partial matching in geospatial conflation: a unified optimization model, ISPRS Int. J. Geo-Inf., 11, 375, https://doi.org/10.3390/ijgi11070375, 2022.

Lesser, G., Roelvink, D., van Kester, J., and Stelling, G.: Development and application of a three-dimensional model for coastal morphology and hydrodynamics, Coast. Eng., 51, 883–915, https://doi.org/10.1016/j.coastaleng.2004.07.014, 2004.

Li, K., Qin, X., Xu, B., Yin, Z., Wu, Y., Mu, G., Wei, D., Tian, X., Shao, H., Wang, C., Jia, H., Li, W., Song, H., Liu, J., and Jiao, Y.: Hydro-climatic aspects of prehistoric human dynamics in the drylands of the Asian interior, Holocene, 33, 194–207, https://doi.org/10.1177/09596836221131694, 2023.

Lisenby, P. E., Fryirs, K. A., and Thompson, C. J.: River sensitivity and sediment connectivity as tools for assessing future geomorphic channel behavior, Int. J. River Basin Manag., 18, 279–293, https://doi.org/10.1080/15715124.2019.1672705, 2020.

Litwin, D. G., Tucker, G. E., Barnhart, K. R., and Harman, C. J.: Catchment coevolution and the geomorphic origins of variable source area hydrology, Water Resour. Res., 60, e2023WR034647, https://doi.org/10.1029/2023WR034647, 2024.

Lu, S. F., Wang, Y. X., Ma, M. Y., and Xu, L.: Water seepage characteristics in porous media with various conduits: Insights from a multi-scale Darcy–Brinkman–Stokes approach, Comput. Geotech., 157, 105317, https://doi.org/10.1016/j.compgeo.2023.105317, 2023.

702 Meyer, K., Hoyer-Leitzel, A., Iams, S., Klasky, I., Lee, V., Ligtenberg, S., Bussmann, E.,
703 and Zeeman, M. L.: Quantifying resilience to recurrent ecosystem disturbances using
704 flow–kick dynamics, Nat. Sustain., 1, 671–678, https://doi.org/10.1038/s41893-018-
705 0168-z, 2018.

706 Morón, S., Edmonds, D., and Amos, K.: The role of floodplain width and alluvial bar
707 growth as a precursor for the formation of anabranching rivers, Geomorphology, 278,
708 78–90, https://doi.org/10.1016/j.geomorph.2016.10.026, 2017.

709 Neuendorf, F., von Haaren, C., and Albert, C.: Assessing and coping with uncertainties in
710 landscape planning: an overview, Landscape Ecol., 33, 861–878,
711 https://doi.org/10.1007/s10980-018-0643-y, 2018.

712 O'Callaghan, J. F. and Mark, D. M.: The extraction of drainage networks from digital
713 elevation data, Comput. Vis. Graph. Image Process., 28, 323–344,
714 https://doi.org/10.1016/S0734-189X(84)80011-0, 1984.

715 O'Neill, B. C., Tebaldi, C., van Vuuren, D. P., Eyring, V., Friedlingstein, P., Hurtt, G.,
716 Knutti, R., Kriegler, E., Lamarque, J.-F., Lowe, J., Meehl, G. A., Moss, R., Riahi, K.,
717 and Sanderson, B. M.: The Scenario Model Intercomparison Project (ScenarioMIP)
718 for CMIP6, Geosci. Model Dev., 9, 3461–3482, https://doi.org/10.5194/gmd-9-3461-
719 2016, 2016.

720 Qu, Y. and Duffy, C. J.: A semidiscrete finite volume formulation for multiprocess
721 watershed simulation, Water Resour. Res., 43, W08419,
722 https://doi.org/10.1029/2006WR005752, 2007.

723 Ranacher, P. and Tzavella, K.: How to compare movement? A review of physical
724 movement similarity measures in geographic information science and beyond,
725 Cartogr. Geogr. Inf. Sci., 41, 286–307, doi:10.1080/15230406.2014.890071, 2014.

726 Schütze, O., Esquivel, X., Lara, A., and Coello, C. A. C.: Using the averaged Hausdorff
727 distance as a performance measure in evolutionary multiobjective optimization, IEEE
728 Trans. Evol. Comput., 16, 504–522, https://doi.org/10.1109/TEVC.2011.2161872,
729 2012.

730 Shao, Y., Gong, H., Elachi, C., Brisco, B., Liu, J., Xia, X., Guo, H., Geng, Y., Kang, S.,
731   Liu, C., Yang, Z., and Zhang, T.: The lake-level changes of Lop Nur over the past
732   2000 years and its linkage to the decline of the ancient Loulan Kingdom, J. Hydrol.
733   Reg. Stud., 40, 101002, https://doi.org/10.1016/j.ejrh.2022.101002, 2022.

734 Tang, Q., Hu, H., Oki, T., and Tian, F.: Water balance within intensively cultivated alluvial
735   plain in an arid environment, Water Resour. Manag., 21, 1703–1715,
736   https://doi.org/10.1007/s11269-006-9121-4, 2007.

737 Tarboton, D. G.: A new method for the determination of flow directions and upslope areas
738   in grid digital elevation models, Water Resour. Res., 33, 309–319,
739   https://doi.org/10.1029/96WR03137, 1997.

740 Temme, A. J. A. M., Heuvelink, G. B. M., Schoorl, J. M., and Claessens, L.: Geostatistical
741   simulation and error propagation in geomorphometry, in: Geomorphometry: Concepts,
742   Software, Applications, edited by: Hengl, T. and Reuter, H. I., Developments in Soil
743   Science, 33, 121–140, https://doi.org/10.1016/S0166-2481(08)00005-6, 2009.

744 Tucker, G. E. and Hancock, G. R.: Modelling landscape evolution, Earth Surf. Process.
745   Landf., 35, 28–50, https://doi.org/10.1002/esp.1952, 2010.

746 Tucker, G., Lancaster, S., Gasparini, N., and Bras, R.: The channel-hillslope integrated
747   landscape development model (CHILD), in: Landscape erosion and evolution
748   modeling, edited by: Harmon, R. S. and Doe, W. W., 349–388,
749   https://doi.org/10.1007/978-1-4615-0575-4_12, 2001.

750 Vrugt, J. A., ter Braak, C. J. F., Diks, C. G. H., Robinson, B. A., Hyman, J. M., and Higdon,
751   D.: Accelerating Markov chain Monte Carlo simulation by differential evolution with
752   self-adaptive randomized subspace sampling, Int. J. Nonlinear Sci. Numer. Simul., 10,
753   273–290, https://doi.org/10.1515/IJNSNS.2009.10.3.273, 2009.

754 Wang, M. and Shen, Z. K.: Present-day crustal deformation of continental China derived
755   from GPS and its tectonic implications, J. Geophys. Res. Solid Earth, 125,
756   e2019JB018774, https://doi.org/10.1029/2019JB018774, 2020.

757 Wang, Y., Zhou, Y., Wu, S., and Peng, X.: Colonize the desert vs. retreat to the mountains:
758   The evolution of city–water relationships in the Tarim river basin over the past 2000

759   years, Appl. Geogr., 170, 103346, https://doi.org/10.1016/j.apgeog.2024.103346,
760   2024.

761   Whipple, K. X., Forte, A. M., DiBiase, R. A., Gasparini, N. M., and Ouimet, W. B.:
762   Timescales of landscape response to divide migration and drainage capture:
763   Implications for the role of divide mobility in landscape evolution, J. Geophys. Res.
764   Earth Surf., 122, 248–273, https://doi.org/10.1002/2016JF003973, 2017.

765   Xu, L., Ma, M. Y., Lan, T. G., Wang, Y. X., and Lu, S.-F.: Exploring soil water retention
766   hysteresis in the entire suction range and microstructure evolution of loess: The
767   influence of sediment depths, Eng. Geol., 328, 107373,
768   https://doi.org/10.1016/j.enggeo.2023.107373, 2024.

769   Yang, R., Willett, S. D., and Goren, L.: In situ low-relief landscape formation as a result
770   of river network disruption, Nature, 520, 526–529,
771   https://doi.org/10.1038/nature14354, 2015.

772   Yu, G. A., Disse, M., Huang, H. Q., Yu, Y., and Li, Z.: River network evolution and fluvial
773   process responses to human activity in a hyper-arid environment – case of the Tarim
774   River in Northwest China, Catena, 147, 96–109,
775   https://doi.org/10.1016/j.catena.2016.06.038, 2016.

776   Zhang, Y., Slingerland, R., and Duffy, C.: Fully-coupled hydrologic processes for
777   modeling landscape evolution, Environ. Model. Softw., 82, 89–107,
778   https://doi.org/10.1016/j.envsoft.2016.04.014, 2016.

779   Zhen, J., Guo, Y., Wang, Y., Li, Y., and Shen, Y.: Spatial–temporal evolution and driving
780   factors of water–energy–food–ecology coordinated development in the Tarim River
781   Basin, J. Hydrol. Reg. Stud., 58, 102288, https://doi.org/10.1016/j.ejrh.2025.102288,
782   2025.

783   Zhou, Y., Gao, Y., Shen, Q., Yan, X., Liu, X., Zhu, S., Lai, Y., Li, Z., and Lai, Z.: Response
784   of channel morphology to climate change over the past 2000 years using vertical
785   boreholes analysis in the Lancang River headwater in the Tibetan Plateau, Water, 14,
786   1593, https://doi.org/10.3390/w14101593, 2022.

787   Zeng, X. and Wu, J.: Numerical simulation of basin-scale river channel migration driven

788   by   landscape   evolution,   HydroShare   [data   set],

789   https://doi.org/10.4211/hs.a6eb2a2c8ae746cf99d5d89a5ed2600b, 2025.

790   Zubovich, A., Schöne, T., Metzger, S., Mosienko, O., Mukhamediev, S., Sharshebaev, A.,

791   and Zech, C.: Tectonic interaction between the Pamir and Tien Shan observed by GPS,

792   Tectonics, 35, 283–292, https://doi.org/10.1002/2015TC004055, 2016.